Molecular Packing Determines Singlet Exciton Fission in Organic Semiconductors

Kolja Kolata, Tobias Breuer, Gregor Witte,* and Sangam Chatterjee*

Faculty of Physics and Materials Sciences Center, Philipps-Universität Marburg, Renthof 5, D-35032 Marburg, Germany

ABSTRACT Carrier multiplication by singlet exciton fission enhances photovoltaic conversion efficiencies in organic solids. This decay of one singlet exciton into two triplet states allows the extraction of up to two electrons per harvested photon and, hence, promises to overcome the Shockley–Queisser limit. However, the microscopic mechanism of singlet exciton fission, especially the relation between molecular packing and electronic response, remains unclear, which therefore hampers the systematic improvement of organic photovoltaic devices. For the model system perfluoropentacene, we experimentally show that singlet exciton fission is greatly enhanced for a slip-stacked molecular arrangement by addressing different crystal axes featuring different packing schemes. This reveals that the fission process strongly depends on the intermolecular coupling: slip-stacking favors delocalization of excitations and allows for efficient exciton fission, while face-to-edge molecular orientations commonly found in the prevailing herringbone molecular stacking patterns even suppress it. Furthermore, we clarify the controversially debated role of excimer states as intermediary rather than competitive or precursory. Our detailed findings serve as a guideline for the design of next-generation molecular materials for application in future organic light-harvesting devices exploiting singlet exciton fission.

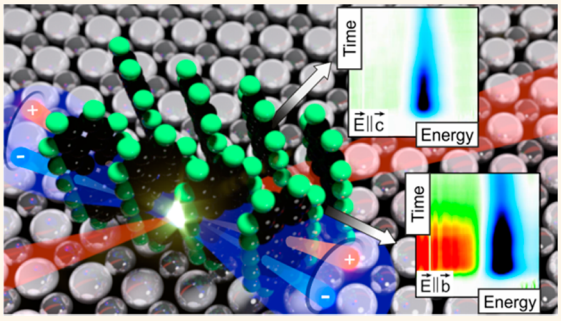

KEYWORDS: singlet exciton fission · π–π-stacking · light harvesting · correlated triplet pair dynamics · ultrafast pump–probe spectroscopy · organic thin films

The key requirements for successful light-harvesting devices are low cost and high energy yields. Organic solids potentially allow for large-area and low-cost printing on flexible substrates[1−3] and, therefore, have lately matured into viable competitors for their well-established inorganic counterparts. Despite the large molecular photon absorption cross-section, the overall efficiency of organic solar cells still remains comparably low. In general, the light-to-current conversion in semiconductors exploits the photovoltaic effect: the absorption of a photon excites an electron, leaving behind a so-called hole; both electron and hole may form a Coulomb correlated electron–hole pair or exciton. A net current is collected once the exciton dissociates at the donor–acceptor interface states, while the excess energy is dissipated as heat. This remaining quantum deficit reduces the maximum energy conversion in conventional solar cells according to the Shockley–Queisser limit.[4] Carrier multiplication schemes can overcome this constraint by using the excess energy to generate additional excited carriers. A prominent example in organic semiconductors is singlet exciton fission, where one singlet exciton (X_{S1}) is converted into two triplet excitons (X_{T1}),[5−7] dipole-forbidden states that do not directly couple to light. Evidently, this process is exothermic when the energy balance fulfills $E(X_{S1}) \geq 2E(X_{T1})$. At least two participating molecules are necessary due to Pauli's exclusion principle; however, this requires effective intermolecular coupling, which is rarely found in van der Waals-bound solids. The prevailing packing motif in the crystalline phase of π-conjugated molecules is the face-to-edge herringbone structure. A prominent representative adopting this arrangement is pentacene, a prototypical organic semiconductor commonly serving as a benchmark system. Regrettably, previous ultrafast experiments devoted to exciton fission were typically performed on polycrystalline samples (see, for example, refs 8 and 9 for recent reviews), as the fabrication of highly ordered thin films yields only microscopically small

* Address correspondence to sangam.chatterjee@physik.uni-marburg.de; gregor.witte@physik.uni-marburg.de.

Received for review May 9, 2014 and accepted June 23, 2014.

Published online June 23, 2014
10.1021/nn502544d

© 2014 American Chemical Society

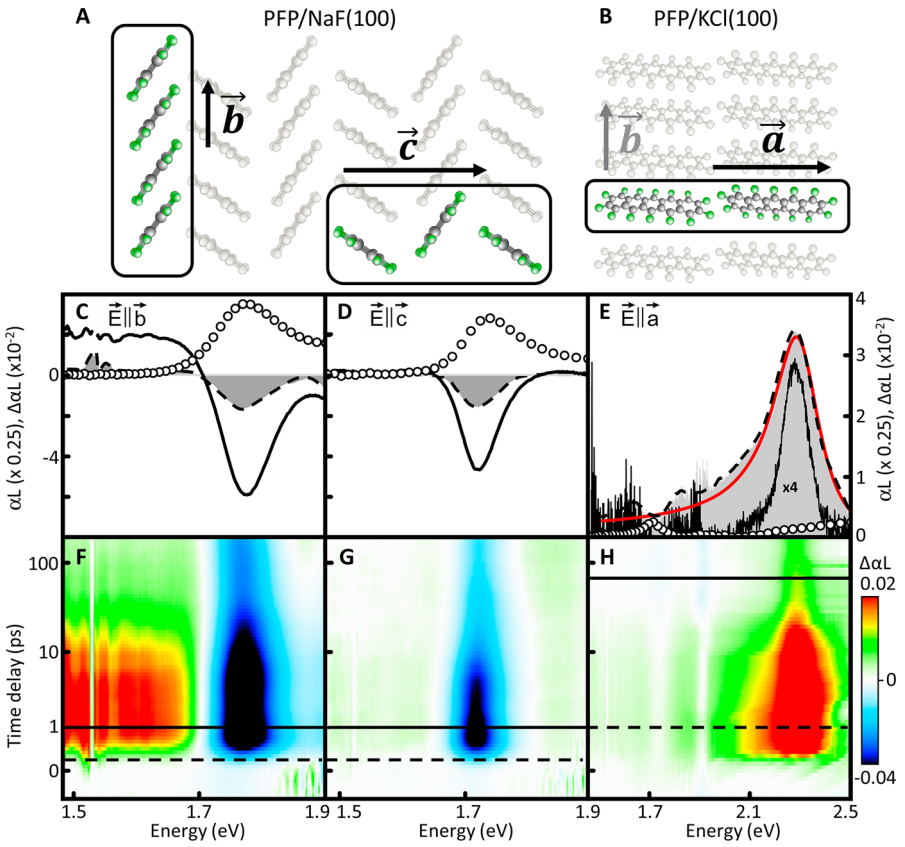

Figure 1. Correlation of packing scheme and optical response along all three crystal axes. Schematic PFP stacking patterns along (A) the $\vec{b}$- and $\vec{c}$-axes on NaF(100) substrates and (B) $\vec{a}$- and $\vec{b}$-axes on KCl(100) substrates (top view). Linear absorption (open circles) along (C) $\vec{b}$-axis, (D) $\vec{c}$-axis, (E) $\vec{a}$-axis and corresponding differential absorption spectra at time delays of 300 fs (dashed) and 1 ps (solid) for the $\vec{b}$- and $\vec{c}$-axes. For the $\vec{a}$-axis, differential absorption spectra at 1 ps (dashed) and 90 ps (solid) are shown together with a Fano fit (red) of the induced absorption. False-color plots: time evolution of the differential absorption spectra along (F) the $\vec{b}$-axis, (G) the $\vec{c}$-axis, and (H) the $\vec{a}$-axis shown on a nonlinear time scale. Signatures at 1.52 eV due to stray light from the laser used for supercontinuum generation are whited out.

single-crystalline domains and, therefore, the crystal axes and excitation dynamics were not correlated. Other packing motifs may enhance the intermolecular coupling, and various synthetic strategies to affect the molecular arrangement are presently pursued.[10] A promising route is stacking the molecules face-to-face, generally referred to as "π-stacking". While a direct coplanar stacking of the molecular planes causes steric repulsion, enhanced intermolecular coupling is expected when the molecules are additionally displaced laterally (termed as slip-stacked packing). Moreover, slip-stacking is predicted to greatly increase the rate of singlet exciton fission, as it breaks the symmetry plane between the stacked molecules, which results in nonvanishing interaction integrals essential for the fission process.[8,9] However, the impact of molecular packing on singlet exciton fission has not been studied due to the lack of sufficiently sized crystallites, which enable directional-resolved optical investigations.

RESULTS AND DISCUSSION

We investigate the relaxation and singlet exciton fission dynamics in perfluoropentacene ($C_{22}F_{14}$, PFP). This particularly well-suited model system features different molecular stacking patterns in different directions within the single crystal. In particular, its layered crystal structure exhibits anisotropic molecular packing within the ($\vec{b}\vec{c}$)-plane, where the molecules are slip-stacked along the $\vec{b}$-axis and aligned in a face-to-edge herringbone arrangement along the $\vec{c}$-axis (*cf.* Figure 1A and B). The herringbone angle of nearly 90° in combination with the intermolecular spacing leads to virtually vanishing interaction between molecules along the face-to-edge direction, leaving solely the slip-stacked molecules along the $\vec{b}$-axis to potentially contribute to singlet exciton fission. Only this rarely found peculiar packing motif allows the unique, precise determination of the structure-dependent electronic responses. Furthermore, density-functional theory (DFT) predicts a pronounced dispersion along this direction in crystalline PFP.[11] Additionally, slip-stacking is expected to enhance the delocalized nature of excitons in organic semiconductors,[12−14] which, in turn, is considered as the primary driving force for singlet exciton fission.[15] Consequently, highly anisotropic singlet exciton fission is expected in PFP crystals. In particular, we exploit the unique epitaxial growth relations of PFP thin films on KCl(100) and NaF(100)

substrates (standing *vs* lying, *cf.* Figure 1A and B).[16] These yield macroscopic single-crystalline domains, which enable polarization-resolved ultrafast transient-absorption experiments along all three crystal axes. Thereby, we here provide first experimental data unambiguously showing the direct correlation of singlet exciton fission with the molecular packing motifs in organic solids.

Already the linear absorption spectra reveal the anisotropic nature of the electronic response in PFP. For simplicity, we refer only to crystal axes instead of the linear polarization state of the probe light set parallel to the respective axis in the following. The lowest energy transitions for the $\vec{b}$-axis (Figure 1C) and the $\vec{c}$-axis (Figure 1D) around 1.7−1.8 eV are associated with singlet excitons X_{S1}. This is about 0.3 eV below the transition from the highest occupied molecular orbital (HOMO) to the lowest unoccupied molecular orbital (LUMO) in solution $S_0 \rightarrow S_1$.[17,18] The corresponding transition-dipole moment is oriented along the short axis of the molecular plane, resulting in negligible absorption signatures along the $\vec{a}$-axis in this energy range (Figure 1E). The anisotropy significantly influences the carrier dynamics monitored by the polarization- and time-resolved differential absorption ($\Delta\alpha L$) shown as false-color plots in Figure 1F, G, and H, for the $\vec{b}$-axis, the $\vec{c}$-axis, and the $\vec{a}$-axis, respectively. For all three cases, the pump pulses are linearly polarized along the $\vec{b}$-axis and tuned to the $S_0 \rightarrow S_1$ transition energy at 2 eV. These data clearly show nonuniform responses despite identical excitation conditions.

First, we focus on the X_{S1} resonance. Exemplary $\Delta\alpha L$ spectra are presented for the $\vec{b}$-axis and for the $\vec{c}$-axis in Figures 1C and D, respectively. Shortly after the excitation (pump−probe time delay Δt = 300 fs), a bleaching of the X_{S1} resonance is found along both axes, which prevails at longer time delays (Δt = 1 ps). Furthermore, a broadband induced absorption (BIA) is observed solely along the $\vec{b}$-axis (Figure 1F). The BIA is a characteristic signature for additional transitions emerging due to the presence of excited carriers. The associated dipole moment is oriented exclusively along the $\vec{b}$-axis, indicating that these excitations are partially delocalized across at least two molecules along this direction, as expected for the slip-stacked packing motif. In addition, we observe broadband luminescence at energies below the X_{S1} resonance for the same excitation conditions which is typically attributed to excimers (*cf.* inset in Figure 2C). This quasi-particle describes an excitation shared between two neighboring molecules, effectively reducing the system's energy. Excimers were originally identified in luminescence spectra in solution,[19−21] and the description was later also transferred to molecular solids.[22,23] Accordingly, we attribute the BIA to transitions between excimer-like states (*EX*) with their transition dipole moments oriented along the $\vec{b}$-axis. This is of particular interest, as the role of excimers in singlet exciton fission is presently debated controversially. Sometimes, they are considered parasitical,[8] while others identify their formation as the mediating mechanism.[24,25]

Next, we discuss the excitation dynamics along the $\vec{a}$-axis (Figure 1E). Here, we observe a strong induced absorption at 2.28 eV. Its peak position corresponds well to the dipole-allowed $T_1 \rightarrow T_4$ transition, where a strong oscillator strength is predicted at 2.16 eV based on single-molecular time-dependent DFT calculations.[26] Intriguingly, the spectral line shape evolves with time. Initially, the asymmetric peak (Δt = 1 ps) resembles a Fano-type resonance. This is typically observed when the transition amplitude associated with a resonance experiences constructive and destructive interference with a continuum of background transitions. Later, the resonance evolves into a symmetric Voigt-like shape (Δt = 90 ps), capturing the associated lifetime, including the inhomogeneity in the sample. This transformation is attributed to the dephasing of the correlated-triplet exciton pair ($^1(TT)$),[27,28] a coherent superposition of two X_{T1} considered to be the intermediate state in the process of singlet exciton fission:[8]

$$X_{S1} \rightarrow {}^1(TT) \rightarrow X_{T1} + X_{T1}$$

The interference of the transition amplitudes from $^1(TT)$ to T_4 results in a Fano-type resonance since the nondegenerate sublevels contributing to $^1(TT)$ act as a quasi-continuum; this interference is lifted once the $^1(TT)$ has dephased.

To clarify the interplay of *EX* and $^1(TT)$, we further analyze the time evolution of the individual spectral signatures. Normalized transients for the $\Delta\alpha L$ signatures are plotted in Figure 2A: the bleaching of the X_{S1} resonance (1.75−1.85 eV) is given as blue open circles, the BIA revealing the *EX* dynamics (1.55−1.75 eV) is displayed as red open circles, both along the $\vec{b}$-axis, while the induced absorption along the $\vec{a}$-axis associated with the $^1(TT)$ (2.24−2.3 eV) is shown as red dots. The rise dynamics of the X_{S1} resonance's bleaching and of the induced absorption along the $\vec{a}$-axis are identical and occur simultaneously within our time resolution, while the BIA sets in later. Therefore, the $^1(TT)$ is formed immediately after excitation and before *EX* is populated. This is consistent with the aforementioned charge-transfer nature of the lowest singlet exciton resonance since charge-transfer excitons are expected to directly couple to $^1(TT)$ as a mediator for singlet exciton fission and *EX* formation.[15,29] At longer time delays, all the transients, including the dynamics along the *c*-axis (*cf.* Figures S10, S11), undergo the same decay dynamics, revealing two distinct time regimes ($\tau_1 = 12 \pm 3$ ps; $\tau_2 = 0.5 \pm 0.3$ ns), connecting all of them.

The comprehensive scenario thus appears as follows: the initial bleaching results from stimulated emission and blocked absorption experienced by the

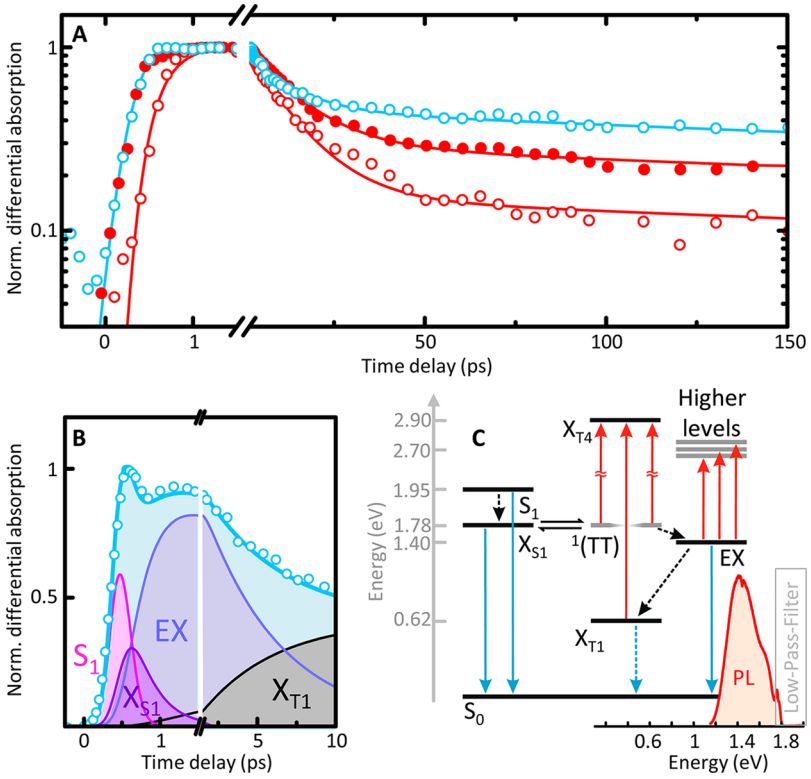

Figure 2. Carrier dynamics and schematics of the rate equation model reproducing the experimental data. (A) Spectrally integrated transients of the bleaching (1.75−1.85 eV, blue open circles) and the BIA (1.55−1.75 eV, red open circles) along the $\vec{b}$-axis as well as induced absorption along the $\vec{a}$-axis (2.24−2.3 eV, red dots). The fast dynamics are modeled by the rate-equation model, while the long-term dynamics are reproduced by double-exponential functions, shown as solid lines. All signals show the same decay constants within the experimental error: $\tau_1 = 12 \pm 3$ ps; $\tau_2 = 0.5 \pm 0.3$ ns. (B) Results of the rate-equation model (solid line). The individual contributions are shown by the shaded areas, while the experimental data are given as open circles. (C) Energy level scheme and underlying relaxation mechanisms implemented in the rate-equation model. The solid blue arrows represent radiative recombination; the dashed arrows, nonradiative relaxation. Red arrows indicate induced absorption. The X_{T1} energy is taken from single-molecular DFT calculations.[33] The inset shows the photoluminescence spectrum of the sample.

probe pulse after the crystal is excited into the coupled X_{S1}-$^1(TT)$ state. This coupled state crosses into the *EX* potential diabatically through a conical intersection,[30−32] and new *EX*-related absorption channels emerge, observed as BIA. At this point, the stimulated emission is reduced due to the vanishing effective overlap between *EX* and S_0 wave functions. However, the bleaching recovers as *EX* inhibits the fundamental absorption $S_0 \rightarrow X_{S1}$, where it blocks at least two transition channels instead of one, manifested in the bleaching dip at $\Delta t = 700$ fs observed in Figure 2B. The decay with a constant of around $\tau_1 = 12 \pm 3$ ps is assigned to the radiative relaxation of *EX* and dephasing of $^1(TT)$, whereas the second, slower decay is attributed to relaxation of X_{T1} into the ground state with a decay constant of $\tau_2 = 0.5 \pm 0.3$ ns. Thus, neither is the $^1(TT)$ formation in competition with *EX* formation nor is *EX* a precursor for the $^1(TT)$ formation, as previously suggested for pentacene.[23] Evaluating the bleaching amplitude ratio of the fundamental transition at short and long delay times, we conclude that two-thirds of $^1(TT)$ recombine radiatively, while one-third act as independent X_{T1}. The relatively high radiative recombination rate indicates that many of the contributing sublevels have a singlet spin-function admixture.[8]

All these observations are implemented into a rate-equation model to quantify the observed dynamics (details are given in the Supporting Information); the included states and mechanisms are summarized in Figure 2C. Results from the simulation are given in Figure 2B as solid lines, yielding excellent agreement with the experimental observations. The ground-state bleaching is modeled by blocked absorption channels due to excited states. Hence, occupation of the S_1, the X_{S1}, the *EX*, and the X_{T1} contributes to the signal. The X_{S1} is mimicked as an X_{S1}-$^1(TT)$ coupled state, since the rigid selection rules for individual molecules are lifted in non-centrosymmetric crystals and the singlet and triplet wave functions combine into new eigenstates.

At early times, the bleaching dynamics are dominated by stimulated emission channels as well as relaxation of excited molecules into singlet excitons ($S_0 \rightarrow X_{S1}$). Remarkably, even the dip in the bleaching of the X_{S1} transition at early times is reproduced. The long-term decay is dominated by radiative recombination of *EX* as well as diffusion into X_{T1}. The same level of agreement is found for identical parameters for

the BIA; here, only *EX* and X_{T1} contribute. Since this signature occurs only as soon as excited, partially delocalized excitons are present in the system, these transitions within the triplet system challenge the prevailing expectation of a strictly localized, Frenkel-type X_{T1}. The associated induced absorption shows pronounced crystalline anisotropies within the $\vec{b}\vec{c}$-plane, where it is observed only along the slip-stacked packing motif of the $\vec{b}$-axis and not found along the face-to-edge packing motif of the $\vec{c}$-axis (*cf.* Figure S11). The partially delocalized triplet excitons corroborate the enhanced coupling between slip-stacked molecules.

CONCLUSIONS

In conclusion, we have observed singlet exciton fission in crystalline PFP along the $\vec{b}$-axis, which is accompanied by formation of an excimer-like state. The formation of the correlated-triplet exciton pair occurs before the formation of the excimer-like states. Its dephasing is manifested by the evolution of an asymmetric Fano-type feature into a symmetric resonance in the induced absorption along the $\vec{a}$-axis. Furthermore, the same decay dynamics are observed for the excimer-related broadband induced absorption features along the $\vec{b}$-axis as well as the ground-state bleaching, undoubtedly connecting all three of them. Hence, coupling between molecules within the $\vec{b}$-axis enhances exciton delocalization, which then itself enhances singlet and triplet level mixing and consequently lifts strict single-molecular selection rules. At later delay times ($\tau > 15$ ps), around one-third of the correlated-triplet exciton pairs diffuse into independent triplet excitons. They remain in an excimer-type state polarized along the $\vec{b}$-axis and decay on a nanosecond time scale. All these observations render PFP single crystals as an ideal model system to study electronic excitation dynamics such as excimer formation and singlet exciton fission with respect to the crystalline molecular packing. This unprecedented correlation between molecular packing motifs and the optical response not only provides detailed insights into the exciton fission dynamics but also serves as an important guideline for the design of future molecular materials for light-harvesting devices.

METHODS

Substrate Preparation and Sample Growth. The alkali halide surfaces were prepared by cleaving slices of about 2 mm thickness from a single-crystal rod (Korth Kristalle GmbH) in air. Subsequently, the samples were transferred into the vacuum system using a load-lock system and annealed at 450 K under vacuum to remove adsorbed water. Subsequently, the highly crystalline PFP (Kanto Denka Kogoyo, purity >99%) thin films (150 nm) were prepared under ultra-high-vacuum conditions by molecular beam deposition onto KCl(100) and NaF(100) surfaces following the general growth procedure described in ref 16. Elevation of the substrate temperature during the deposition process leads to enhanced crystallinity of the adsorbed layers as well as increasing size of uniformly oriented domains (Figure S1). Therefore, the samples investigated in this report were deposited at a substrate temperature of 350 K. At this temperature, the sticking coefficient is not yet reduced and the domain size is maximized. The molecules assemble in an upright fashion with their $\vec{b}$- and $\vec{c}$-axes parallel to the surface on NaF(100) (Figure S2A), while a recumbent orientation is adopted on KCl(100), yielding the $\vec{a}$- and the $\vec{b}$-axes of the PFP lattice parallel to the substrate surface (Figure S2B).

Structural Investigations. The film morphology was characterized by atomic force microscopy (AFM, Agilent SPM 5500) operated in tapping mode at ambient conditions and room temperature. AFM tips with resonance frequencies of about 325 kHz, radii of 7 nm, and force constants of 40 N/m were used. Exemplary film morphologies are depicted in Figure S1. These reveal that appropriate preparation conditions lead to nucleation of elongated islands with preferred orientations along the NaF ⟨100⟩ and KCl ⟨110⟩ directions. Due to the 4-fold symmetry of the substrates, four 90°-rotated domains are found.

X-ray diffraction (XRD) measurements were applied to analyze the exact crystalline structure. The crystalline orientation of the samples was determined from XRD data acquired with a Bruker D8 Discovery diffractometer using Cu Kα radiation (λ = 1.54056 Å) and a silicon strip detector. Bragg−Brentano scans of PFP/NaF(100) are given in Figure S2A; the PFP(*n*00) diffraction peaks are clearly observed. These lattice planes correspond to uprightly oriented molecules, as shown schematically in the inset. Additionally, azimuthal scans of lattice planes that are not parallel to the substrate have been performed to determine the exact lateral arrangement. A scan of the PFP(112) and (11−2) lattice planes (which are recorded simultaneously due to their similar lattice spacing) yields 16 peaks. After elimination of the peaks resulting from the 4-fold symmetry and the mirror domains, two peaks with a mutual splitting of $\Delta\Phi = 3.1°$ remain.

Subsequent consideration of the relative orientation between the projection of the lattice plane onto the PFP(100) lattice plane allows us to determine the orientation of the unit cell axes on the surface. This yields that the molecular $\vec{b}$-axis is oriented along the [100] directions of the substrate with a slight misorientation of $\Phi = \pm 1.55°$. This also corresponds to an equivalent orientation along the ⟨100⟩ directions of the PFP $\vec{c}$-axis due to the perpendicular angle between the $\vec{b}$- and $\vec{c}$-axes in the PFP unit cell. The epitaxial alignment of the film as well as the slight misorientation are attributed to the nearly perfectly equivalent values of the PFP $\vec{c}$-axis (4.49 Å) and the distance of two sodium atoms along the NaF ⟨100⟩ directions (4.62 Å).

Supplementary Figure 2B presents the X-ray diffraction patterns of PFP deposited on KCl(100). Here, the (102) peak is observed, which corresponds to a lying orientation of the molecules. An evaluation of the azimuthal distribution of (012) and (01−2) peak intensities yields that the molecular $\vec{b}$- and $\vec{a}$-axes are oriented along the substrate's ⟨110⟩ directions. Due to the very good agreement of the distance between two potassium atoms along ⟨110⟩ (d_{KK}, 4.45 Å) and the molecular $\vec{b}$-axis (4.49 Å), this alignment is found without additional splitting along the surface direction. The adoption of a recumbent orientation on this surface is attributed to higher order commensurability in another direction: $15d_{KK} = |4a_{PFP} - 2c_{PFP}|$. As a consequence, it is possible to address the individual transition dipole moments along the three crystalline axes in PFP within these domains, as it has been previously exploited to characterize the vibronic Davydov splitting.[34] More details on the structural characterization are presented in ref 16.

Due to their relative rotation by 90° resulting from the 4-fold symmetry of the substrate, the signals from the different domains average each other out in polarization-resolved measurements of the ensemble with low spatial resolution. However, the size of the single-crystalline regions is sufficient to allow the exclusive illumination of individual domains when the spot

diameter is small enough. As our setup comprises typical spot diameters of less than 30 μm, such polarization-resolved measurements and therefore exact correlations between molecular arrangement and spectroscopic signature are possible. The differences in the absorption signatures arise from the distinct orientation of the transition dipole moments corresponding to the individual excitations; consequently they lead to a clear color contrast in polarized optical microscopy revealing the large individual domains (Figure S2E and F).

Femtosecond-Pump Supercontinuum-Probe Spectroscopy. We perform ultrafast polarization-resolved pump−probe experiments at room temperature, with sub-300 fs time resolution to study the carrier relaxation dynamics. The schematics of the experiment are sketched in Supplementary Figure S3. The laser source driving the pump and probe is a regenerative 100 kHz Ti:sapphire amplifier system. The samples are excited by strong pump pulses generated in an optical parametric amplifier tuned to 2 eV, corresponding to the gap between the HOMO and the LUMO of the single molecule.[17,18] The photon flux is set to 4.5×10^{15} photons/cm^2 per pulse. A weak femtosecond-white-light supercontinuum is used as a probe. It is generated in an yttrium−aluminum−garnet crystal using a small fraction of the fundamental 800 nm pulse intensity. The linear polarization of both arms, *i.e.*, pump and probe, is defined by combinations of two Glan-laser-type polarizers and broadband half-wave plates set to the desired angle with respect to the plane of incidence before they are focused onto the sample. This way, polarization contrast better than 1000:1 is ensured in both cases. Furthermore, the angle of incidence of the pump pulse is kept small, so that out-of-plane excitations are negligible.

The linear absorption at the excitation energy 2 eV is nearly degenerate for the $\vec{b}$- and the $\vec{c}$-axis. Therefore, for all experiments, the pump pulse is kept linearly polarized along the $\vec{b}$-axis. The probe polarization is adjusted by checking the spectral shift of the fundamental transition in the transmission spectrum (*cf.* Figure S8). The maximum blue-shift in this transition corresponds to the $\vec{b}$-axis response of the crystal. Moreover, the amount of shift as well as the line width of the fundamental transition are very good indicators of the domain quality. The orientation of the probe pulse polarization allows for the correlation of structural properties and electronic excitation. Its polarization is thus set parallel to the $\vec{b}$- and $\vec{c}$-axes for the samples grown on NaF and along the $\vec{a}$- and $\vec{b}$-axes for the samples grown on KCl.

After passing through the sample, the probe is dispersed in a spectrometer with a spectral resolution of 1 nm and is detected by a thermoelectrically cooled silicon charged coupled device camera (1064 × 120 pixels) cooled to −30 °C. The change of absorption is measured by opening and closing the pump and probe arm with mechanical shutters.

Conflict of Interest: The authors declare no competing financial interest.

Supporting Information Available: Atomic force microscopy micrographs visualizing the surface morphology, X-ray diffraction data confirming the molecular orientation, description of the experimental data evaluation procedure including dechirping procedure and crystal-domain selection; discussion of the picosecond carrier dynamics and decay as well as of the triplet dynamics, in-detail description of the rate-equation model. This material is available free of charge *via* the Internet at http://pubs.acs.org.

Acknowledgment. We thank U. Höfer for access to the regenerative Ti:sapphire amplifier system. Financial support is provided by the German Science Foundation (DFG) through the collaborative research center "Structure and Dynamics of Internal Interfaces" (SFB 1083).

REFERENCES AND NOTES

1. Piner, R. D.; Xu, J. Z.; Hong, S.; Mirkin, C. A. "Dip-Pen" Nanolithography. *Science* **1999**, *283*, 661–663.
2. Sirringhaus, H.; Kawase, T.; Friend, R. H.; Shimoda, T.; Inbasekaran, M.; Wu, W.; Woo, E. P. High-Resolution Inkjet Printing of All-Polymer Transistor Circuits. *Science* **2000**, *290*, 2123–2126.
3. Krebs, F. C.; Gevorgyan, S. A.; Alstrup, J. A Roll-to-Roll Process to Flexible Polymer Solar Cells: Model Studies, Manufacture and Operational Stability Studies. *J. Mater. Chem.* **2009**, *19*, 5442–5451.
4. Shockley, W.; Queisser, H. J. Detailed Balance Limit of Efficiency of pn Junction Solar Cells. *J. Appl. Phys.* **1961**, *32*, 510–519.
5. Swenberg, C. E.; Stacy, W. T. Bimolecular Radiationless Transitions in Crystalline Tetracene. *Chem. Phys. Lett.* **1968**, *2*, 327–328.
6. Congreve, D. N.; Lee, J.; Thompson, N. J.; Hontz, E.; Yost, S. R.; Reusswig, P. D.; Bahlke, M. E.; Reineke, S.; Van Voorhis, T.; Baldo, M. A. External Quantum Efficiency above 100% in a Singlet-Exciton-Fission-Based Organic Photovoltaic Cell. *Science* **2013**, *340*, 334–337.
7. Walker, B. J.; Musser, A. J.; Beljonne, D.; Friend, R. H. Singlet Exciton Fission in Solution. *Nat. Chem.* **2013**, *5*, 1019–1024.
8. Smith, M. B.; Michl, J. Singlet Fission. *Chem. Rev.* **2010**, *110*, 6891–6936.
9. Smith, M. B.; Michl, J. Recent Advances in Singlet Fission. *Annu. Rev. Phys. Chem.* **2013**, *64*, 361–386.
10. Anthony, J. E. The Larger Acenes: Versatile Organic Semiconductors. *Angew. Chem., Int. Ed.* **2008**, *47*, 452–483.
11. Delgado, M. C. R.; Pigg, K. R.; da Silva Filho, D. A.; Gruhn, N. E.; Sakamoto, S.; Suzuki, T.; Osuna, R. M.; Casado, J.; Hernández, V.; Teodomiro López Navarrete, J.; *et al*. Impact of Perfluorination on the Charge-Transport Parameters of Oligoacene Crystals. *J. Am. Chem. Soc.* **2009**, *131*, 1502–1512.
12. Tiago, M. L.; Northrup, J. E.; Louie, S. G. *Ab Initio* Calculation of the Electronic and Optical Properties of Solid Pentacene. *Phys. Rev. B* **2003**, *67*, 115212.
13. Sharifzadeh, S.; Biller, A.; Kronik, L.; Neaton, J. B. Quasiparticle and Optical Spectroscopy of the Organic Semiconductors Pentacene and PTCDA from First Principles. *Phys. Rev. B* **2012**, *85*, 125307.
14. Sharifzadeh, S.; Darancet, P.; Kronik, L.; Neaton, J. B. Low-Energy Charge-Transfer Excitons in Organic Solids from First-Principles: The Case of Pentacene. *J. Phys. Chem. Lett.* **2013**, *4*, 2197–2201.
15. Beljonne, D.; Yamagata, H.; Brédas, J. L.; Spano, F. C.; Olivier, Y. Charge-Transfer Excitations Steer the Davydov Splitting and Mediate Singlet Exciton Fission in Pentacene. *Phys. Rev. Lett.* **2013**, *110*, 226402.
16. Breuer, T.; Witte, G. Epitaxial Growth of Perfluoropentacene Films with Predefined Molecular Orientation: A Route for Single-Crystal Optical Studies. *Phys. Rev. B* **2011**, *83*, 155428.
17. Sakamoto, Y.; Suzuki, T.; Kobayashi, M.; Gao, Y.; Fukai, Y.; Inoue, Y.; Sato, F.; Tokito, S. Perfluoropentacene: High-Performance p-n Junctions and Complementary Circuits with Pentacene. *J. Am. Chem. Soc.* **2004**, *126*, 8138–8140.
18. Hinderhofer, A.; Heinemeyer, U.; Gerlach, A.; Kowarik, S.; Jacobs, R. M. J.; Suzuki, T.; Schreiber, F. Optical Properties of Pentacene and Perfluoropentacene Thin Films. *J. Chem. Phys.* **2007**, *127*, 194705.
19. Förster, Th.; Kasper, K. Ein Konzentrationsumschlag der Fluoreszenz. *Z. Phys. Chem.* **1954**, *1*, 275–277.
20. Stevens, B.; Hutton, E. Radiative Life-Time of the Pyrene Dimer and the Possible Role of Excited Dimers in Energy Transfer Processes. *Nature* **1960**, *186*, 1045–1046.
21. Stevens, B. Evidence for the Photo-Association of Aromatic Hydrocarbons in Fluid Media. *Nature* **1961**, *192*, 725–727.
22. Schwoerer, M.; Wolf, H. C. *Organic Molecular Solids*; Wiley-VCH Verlag: Weinheim, 2007; p 156.
23. Schlettwein, D.; Back, A.; Schilling, B.; Fritz, T.; Armstrong, N. R. Ultrathin Films of Perylenedianhydride and Perylenebis(dicarboximide) Dyes on (001) Alkali Halide Surfaces. *Chem. Mater.* **1998**, *10*, 601–612.
24. Zimmerman, P. M.; Zhang, Z.; Musgrave, C. B. Singlet Fission in Pentacene through Multi-Exciton Quantum States. *Nat. Chem.* **2010**, *2*, 648–652.
25. Marciniak, H.; Fiebig, M.; Huth, M.; Schiefer, S.; Nickel, B.; Selmaier, F.; Lochbrunner, S. Ultrafast Exciton Relaxation in

Microcrystalline Pentacene Films. *Phys. Rev. Lett.* **2007**, *99*, 176402.
26. Anger, F.; Ossó, J. O.; Heinemeyer, U.; Broch, K.; Scholz, R.; Gerlach, A.; Schreiber, F. Photoluminescence Spectroscopy of Pure Pentacene, Perfluoropentacene, and Mixed Thin Films. *J. Chem. Phys.* **2012**, *136*, 054701.
27. Chan, W.-L.; Ligges, M.; Jailaubekov, A.; Kaake, L.; Miaja-Avila, L.; Zhu, X.-Y. Observing the Multiexciton State in Singlet Fission and Ensuing Ultrafast Multielectron Transfer. *Science* **2011**, *334*, 1541–1545.
28. Chan, W.-L.; Ligges, M.; Zhu, X.-Y. The Energy Barrier in Singlet Fission Can Be Overcome through Coherent Coupling and Entropic Gain. *Nat. Chem.* **2012**, *4*, 840–845.
29. Shirai, S.; Iwata, S.; Tani, T.; Inagaki, S. *Ab Initio* Studies of Aromatic Excimers Using Multiconfiguration Quasi-Degenerate Perturbation Theory. *J. Phys. Chem. A* **2011**, *115*, 7687–7699.
30. Warshel, A.; Karplus, M. Semiclassical Trajectory Approach to Photoisomerization. *Chem. Phys. Lett.* **1975**, *32*, 11–17.
31. Nikitin, E. E. Theory of Non-Adiabatic Vibrational Relaxation in Atom-Molecular Collisions. *Mol. Phys.* **1964**, *7*, 389–396.
32. Polli, D.; Altoè, P.; Weingart, O.; Spillane, K. M.; Manzoni, C.; Brida, D.; Tomasello, G.; Orlandi, G.; Kukura, P.; Mathies; *et al.* Conical Intersection Dynamics of the Primary Photoisomerization Event in Vision. *Nature* **2010**, *467*, 440–443.
33. Zhang, X.; Li, Q.-S.; Xie, Y.; Schaefer, H. F. The Lowest Triplet Electronic States of Polyacenes and Perfluoropolyacenes. *Mol. Phys.* **2007**, *105*, 2743–2752.
34. Breuer, T.; Celik, M. A.; Jakob, P.; Tonner, R.; Witte, G. Vibrational Davydov-Splittings and Collective Mode Polarizations in Oriented Organic Semiconductor Crystals. *J. Phys. Chem. C* **2012**, *116*, 14491–14503.